

Research Article

Time-Frequency Characterization of Rotating Instabilities in a Centrifugal Pump with a Vaned Diffuser

G. Pavesi, G. Cavazzini, and G. Ardizzon

Department of Mechanical Engineering, University of Padova, Via Venezia 1, 35131 Padova, Italy

Correspondence should be addressed to G. Pavesi, giorgio.pavesi@unipd.it

Received 8 May 2008; Accepted 7 August 2008

Recommended by Eddie Ng

This paper presents acoustic and flowdynamic investigations of large-scale instabilities in a radial pump with a vaned diffuser. Pressure fluctuations were measured with transducers placed flush at the inlet duct, at the impeller discharge, and in the vane diffuser walls. Two impeller rotation speeds were analyzed in the study, at design, and at off-design flow rates. A spectral analysis was carried out on the pressure signals in frequency and in time-frequency domains to identify precursors, inception, and evolution of the pressure instabilities. The results highlighted the existence of a rotating pressure structure at the impeller discharge, having a fluid-dynamical origin and propagating both in the radial direction and inside the impeller. The experimental data were then compared with the results obtained with help of ANSYS CFX computer code; focusing on the changing flow field at part load. Turbulence was reproduced by DES model.

Copyright © 2008 G. Pavesi et al. This is an open access article distributed under the Creative Commons Attribution License, which permits unrestricted use, distribution, and reproduction in any medium, provided the original work is properly cited.

1. INTRODUCTION

Flow in the diffuser pump is dominated by unsteady interactions due to the relative motion and close proximity between the rotating impeller and stationary diffuser, thus, resulting in pressure and velocity fluctuations both upstream and downstream. In the literature, different analytical and experimental approaches were used to investigate the mutual influence of the impeller and its surroundings.

Experiments were conducted to measure pressure fluctuations in diffuser radial pumps by Arndt et al. [1, 2], Furukawa et al. [3] and Guo and Maruta [4], and the details of wake transport across the rotor were tracked in continuously running facilities thanks to LDV and PIV [5–8].

The noise spectral content for studying the unsteady phenomena developing in the impeller passages and at the flow discharge was also considered by researchers. Cumpsty [9] and Neise [10] focused the attention on the tonal pulse generation, whereas Mongeau [11], Mongeau et al. [12], Choi [13], Choi et al. [14], and Bent [15] showed that the flow structure was associated with the dominant unsteadiness of the spectral content at the impeller discharge.

Notwithstanding Ferrara et al. [16] and Horodko [17, 18] demonstrated the applicability of the signal processing

technique waterfalls, based on the time-frequency analysis, to the turbomachinery field, few researchers utilized the most advanced time-frequency analysis technique in the field of turbomachinery.

The objective of this research was to identify and characterize the unsteady phenomena produced in a centrifugal pump, utilizing the Fourier approach and the time-frequency analysis. A correlation between the fluid dynamics and the emitted noise was investigated in order to define the characteristic frequencies of the unsteady stator/rotor interaction.

The paper reports time-resolved fluctuations of pressure upstream and downstream of a radial vaned pump at design flow rate and at low-flow rates. Particular emphasis was dedicated to understand the source of the pitch-wise variations at the impeller outlet and in the diffuser channels.

Furthermore, this paper discusses the numerical data obtained with the ANSYS CFD 11 code, and shows comparison between the theoretical and experimental results on the impeller model equipped with vaned diffuser.

2. TEST FACILITIES

The experimental analysis was performed in the Open Turbomachinery Facility (OTF), in the Department of

TABLE 1

Impeller data				
D_2/mm	B_2/mm	n_b	$\beta_{2c}/^\circ$	φ_{Des}
400	40	7	26.5	.125
Adjustable guide-diffuser vanes data				
D_3/mm	B_3/mm	n_b	$\alpha_{3c}/^\circ$	
410	40	22	21.8	

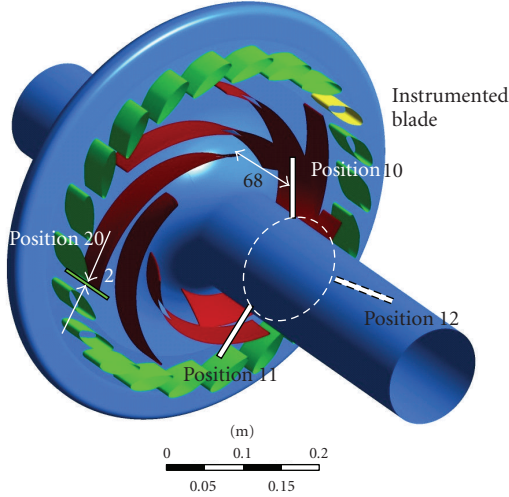


FIGURE 1: Scheme of the impeller and the vaned diffuser.

Mechanical Engineering, University of Padua. The OTF is a water test rig designed for testing the influence of several parameters on the overall performances of both pumps and turbines. The analyzed pump had an original configuration, constituted by a 3D impeller, coupled with a vaned diffuser and a vaned return channel, reproducing the first stage of a two-stage pump turbine ($n_s = 37.6 \text{ m}^{0.75} \text{ s}^{-1.5}$) [19]. The pump configuration was modified to operate with an axial symmetric vaneless return channel, to remove the noise sources due to two stator rows interaction. Table 1 reports the diameter, the width, and the blade angle of the tested pump, as well as the flow coefficient at design point.

Pressure transducers, placed flush with the wall, at different positions carried out measurements of the unsteady pressure. Figure 1 shows a schematic view of the tested configuration with the reference marks of the measurement locations as follows:

- (i) three traverse planes, 68 mm upstream the impeller, in the inlet duct (positions 10, 11, and 12—white marks in Figure 1);
- (ii) a traverse plane, 2 mm downstream the impeller (position 20—green mark in Figure 1);
- (iii) twelve pressure points in the mid height (Figure 2) of a diffuser blade (yellow one in Figure 1).

Piezoelectric dynamic pressure transducers (sensitivity of 76.89 V/Pa) were placed circumferentially equidistant in the inlet duct (positions 10, 11, and 12); and a piezoelectric transducer (sensitivity of 7.62 V/Pa) was located

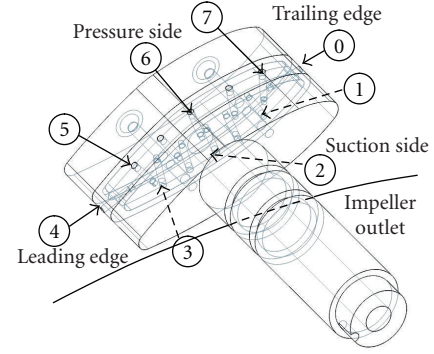


FIGURE 2: Scheme of the diffuser blade with the 12 micro transducers, 7 of them numbered.

2 mm downstream the impeller (position 20). Miniaturized piezoresistive transducers (sensitivity of about 0.29 V/Pa) were placed in the diffuser vane. The sensors' combined nonlinearity, hysteresis, and repeatability were better than $\pm 0.1\%$.

The vibrations of the rig were also measured by accelerometers fixed at the inflow and outflow pump casing, and in the dynamo that powered the pump (charge sensitivity of 0.295 pC/ms^{-2}).

The pump inflow was connected to a water reservoir, filled continuously to a weir brim by an external pump, so that the water level change during operations could be considered negligible. The vibrations of the tank were monitored by an accelerometer.

The data were simultaneously acquired from all the channels at a sampling rate of 2048 Hz and recorded by a workstation controlled transient data recorder, with a dynamic range of 24 bit. The outputs from the transducers channel were conditioned with a low-pass filter at 1024 Hz.

Design and off-design conditions, and two impeller rotation speeds ($n = 500 \text{ rpm}$; 600 rpm) were investigated.

3. SIGNAL PROCESSING

The pressure signals were analyzed both in the frequency domain and in the time-frequency domains.

Auto-spectral and cross-spectral matrices were computed by partitioning each time signal into 256, nonoverlapping segments of 2^{15} samples, filtered with a Hanning window for avoiding aliasing and leakage errors. The frequency resolution was 0.125 Hz. The auto-spectra and the cross-spectra were determined from the following equation:

$$G_{xy}(f) = \frac{1}{NW_H} \sum_{k=1}^N [X_k^*(f)Y_k(f)], \quad (1)$$

where N is the number of segments (i.e., $N = 256$), W_H is weighting constant corresponding to the Hanning window, $Y_k(f)$ is the fast Fourier transform of the k th data segment, and of the signal y and $X_k(f)^*$ is the complex conjugate of the fast Fourier transform of the k th data segment of the signal x . The number of the time segments ($N = 256$) was established, as twice the lowest values whose increase did

not involve a significant variation in the resulting function $G_{ij}(f)$.

The coherence function $\gamma^2(f)$

$$\gamma^2(f) = \frac{|G_{xy}(f)|^2}{G_{xx}(f) \cdot G_{yy}(f)} \quad (2)$$

between two signals was also considered. The square cross-spectrum G_{xy} was divided by the product of the auto-spectra (G_{xx}, G_{yy}) of the signals to measure the degree of linearity between the two signals versus the frequency in the normalized range 0 and 1.

The signal processing in the frequency domain allows finding and analyzing the spectral components contained in the measured pressure signals, but it does not allow an assignment of these spectral components to time. In order to provide information about their time evolution, a time-frequency analysis was carried out by means of the wavelet transforms. For the time-frequency analysis the continuous wavelet transform $W_n(s)$ of the discrete sampled pressure signal x_n was computed via the FFT-based fast convolution:

$$W(s, n) = \sum_{k=0}^{N-1} X_k \left(\sqrt{\frac{2\pi s}{\delta t}} \Psi_0^*(s\omega_k) e^{i\omega_k n \delta t} \right), \quad (3)$$

where X_k is the discrete Fourier transform (DFT) of x_n , k is the frequency index, N is the data series length, s is the wavelet scale, δt is the sampling interval, n is the localized time index, $\Psi_0^*(s\omega_k)$ is the complex conjugate of the Fourier transform of the translated and scaled version of the ‘‘mother wavelet’’ $\Psi(t)$, and ω_k is the angular frequency (if $k \leq N/2$, $\omega_k = 2\pi k/N\delta t$, else $\omega_k = -2\pi k/N\delta t$). The equation contains a normalization factor $\sqrt{2\pi s/\delta t}$ to obtain unit energy at each scale. The choice of the best mother wavelet, which is the basic form of the wavelet function from which dilated and translated versions are derived and used in the wavelet transform, depends on several factors [20]. In this paper, the complex Morlet wavelet (with $2\pi f_0 = 6$) was chosen, since it provided a good balance between time and frequency localization and it returned information about both amplitude and phase.

In order to determine the relation between two pressure signals $x(t)$ and $y(t)$ in the time-frequency domains, the wavelet cross-correlation function, defined by Li [21], was introduced:

$$WC_{x,y}(s, \tau) = \lim_{T \rightarrow \infty} \frac{1}{T} \int_{-T/2}^{T/2} W_x^*(s, b) W_y(s, b + \tau) db, \quad (4)$$

where τ is the time delay between the two signals, W_y is the continuous wavelet transform of $y(t)$, W_x^* is the complex conjugate of the continuous wavelet transform of $x(t)$, b is the location, and s is the scale. In particular, for two sampled pressure signals x_n and y_n with wavelet transforms $W_x(s, n)$ and $W_y(s, n)$, the cross-wavelet spectrum was determined as

$$W_{xy}(s, n) = W_x(s, n) W_y^*(s, n), \quad (5)$$

where $W_y^*(s, n)$ is the complex conjugate of $W_y(s, n)$ [22].

Finally, the wavelet coherence function, measuring the coherence between two sampled signals x_n and y_n both in frequency bands and in time intervals, was considered:

$$R^2(s, n) = \frac{|\langle W_{xy}(s, n) \rangle|^2}{\langle |W_x(s, n)|^2 \rangle \cdot \langle |W_y(s, n)|^2 \rangle}, \quad (6)$$

where $\langle \cdot \rangle$ indicates a smoothing, done using a weighted running convolution in both the time and scale directions, that depends on the mother wavelet [22, 23]. For the complex Morlet wavelet function, the time smoothing was done using the absolute value of the wavelet function at each scale, normalized to have a total weight of unity, with a Gaussian $e^{-t^2/(2s^2)}$. The scale smoothing was done using a boxcar filter of width $\delta j_0 = 0.60$, that is the empirically determined scale decorrelation length. The smoothed real (\Re) and imaginary (\Im) parts of the numerator of (5) were used for determining the wavelet-coherence phase difference:

$$\phi(s, n) = \tan^{-1} \left\{ \frac{\Im[\langle W_{xy}(s, n) \rangle]}{\Re[\langle W_{xy}(s, n) \rangle]} \right\}. \quad (7)$$

4. NUMERICAL PROCEDURE

The commercial software package ANSYS CFX 11.0 was used for performing the numerical simulations on the entire machine. On both blades and wall surfaces, the boundary layer was assumed fully turbulent.

The detached eddy simulation (DES) model was chosen as turbulence model. The shear stress transport $k-\omega$ model covered the boundary layer while the Smagorinsky-lilly model was applied in detached regions.

Since one of the interesting analysis aspects is the possible prediction of noise and vibrations due to stator-rotor interaction, the LES peculiarity of providing information on turbulent flow structures and spectral distribution is useful.

An unsteady model was used for all the computations. For the interface between stator/rotor blocks, the standard transient sliding interface approach was chosen.

The scheme adopted for the time discretization was a second-order implicit time stepping. The time step definition was based on the impeller rotation and it was of about one degree. So, the RMS courant number was $CFL = 2.04$. A maximum number of five iterations were fixed for each time step, resulting in a mass residue of 10^{-6} , momentum residues of 10^{-4} , and turbulence kinetic energy and energy dissipation residues of 10^{-4} .

The numerical data were acquired between the 2nd and 3rd impeller revolution subsequent to the cyclic behavior of the residual plots obtained after about 3 impeller revolutions.

An H-type grid was used for the impeller, whereas an O-type grid was adopted for the diffuser. The leakage from the labyrinth seal was also considered and several H-blocks were built to describe the cavities. The grid, globally of $5.2 \cdot 10^6$ points, (stage inlet 700,000 grid points, impeller 1700,000 grid points, vaned diffuser 1250,000 grid points, return channel 1100,000 grid points, and leakage 400,000) was used to compute the flow in the impeller passages, with y^+ values below 80 in the whole computational region.

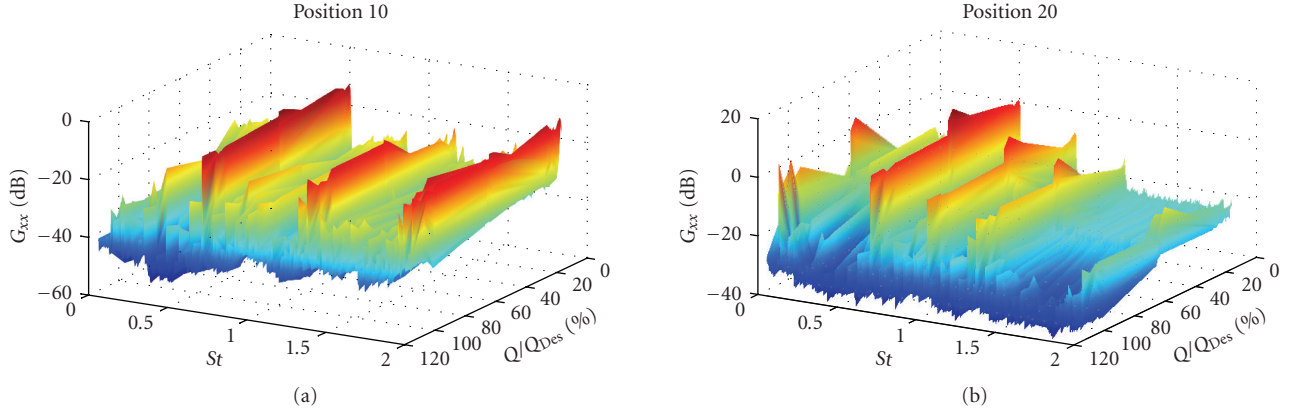


FIGURE 3: Power spectrum of the pressure measured at the pump inlet and outlet at 500 rpm.

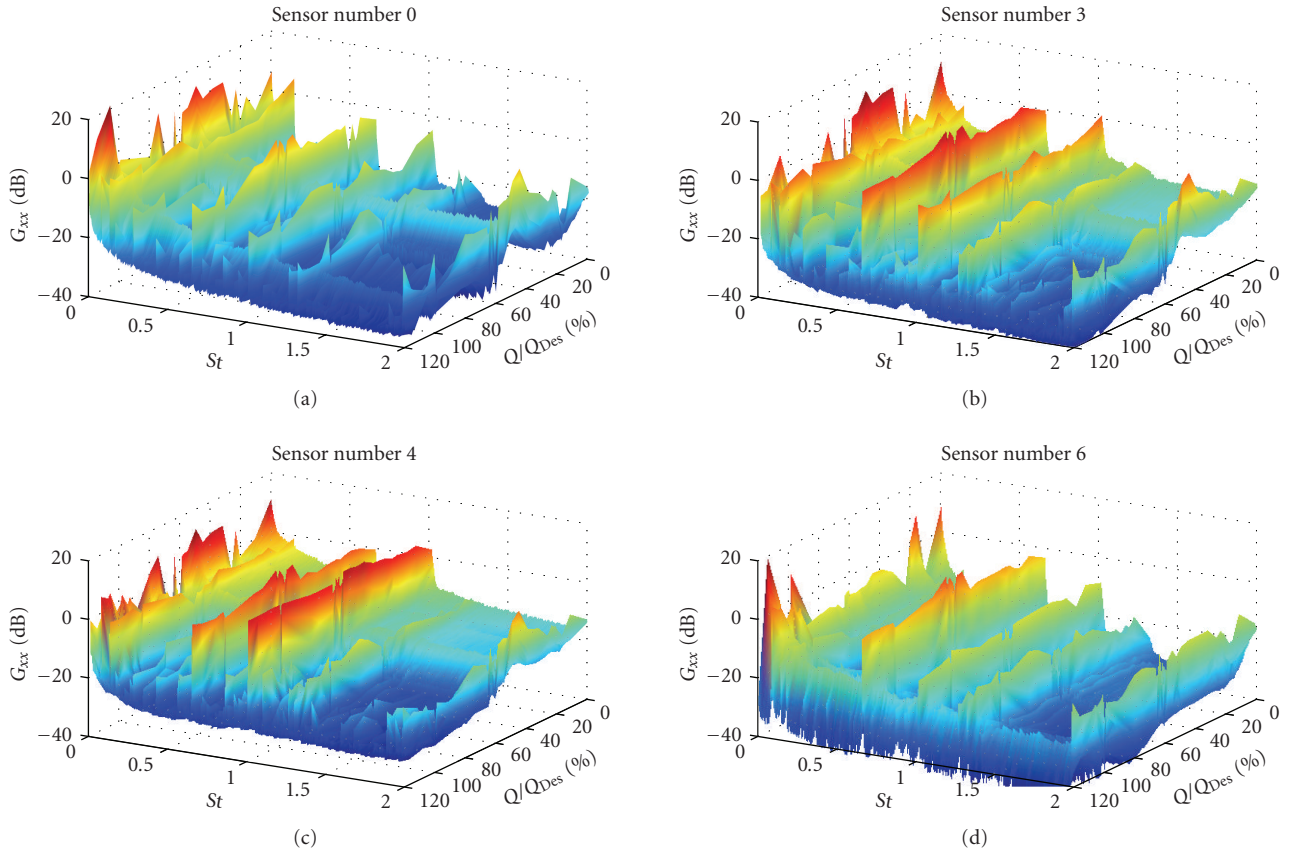


FIGURE 4: Power spectrum of the pressure measured in the diffuser vane at 500 rpm.

As regards the boundary conditions, mass flow rates were prescribed with stochastic fluctuations of the velocities with 5% free-stream turbulence intensity at the pump inlet. At the pump outlet the average static pressure was fixed.

5. RESULTS

Stator rotor interaction gave rise to a complex pressure pulsation system.

Figures 3, 4, and 5 report the power spectra of the unsteady pressure, measured in the impeller inlet and outlet and in some of the microtransducers placed in the diffuser blade versus the Strouhal number ($St = \pi D_2 / n_b f / U_2$).

The spectra were dominated by the blade passage frequency BPF ($St_{BPF} = 1, 2, 3, \dots$) and two subtonal peaks: the main one at $St_F = 0.664$ for both impeller speeds, and the second one at a frequency of about 5 Hz ($St_S = 0.086$ at 500 rpm and $St_S = 0.071$ at 600 rpm). All other

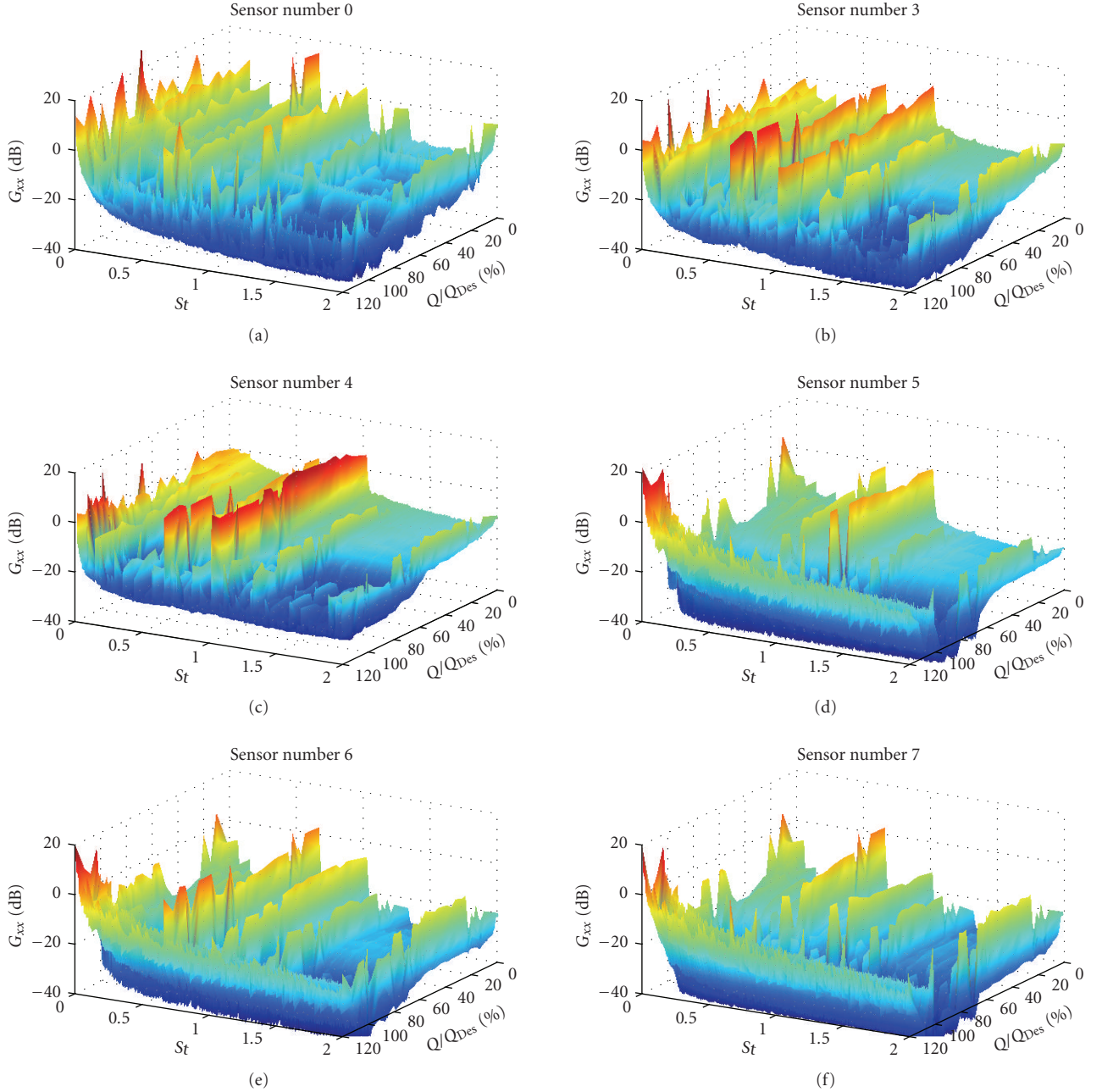


FIGURE 5: Power spectrum of the pressure measured in the diffuser vane at 600 rpm.

peaks in the spectra were harmonics of these fluctuations or nonlinear components, generated by the interaction between the subtonal pressure pulsations' frequency and the BPF:

$$a \cdot St_{F,S} \pm b \cdot St_{BPF}, \quad (a, b \text{ integer}), \quad (8)$$

or between the same two subtonal pressure pulsations frequency $St_F = 0.664$ and $St_S = 0.086$ or $St_S = 0.071$

$$c \cdot St_F \pm d \cdot St_S, \quad (c, d \text{ integer}). \quad (9)$$

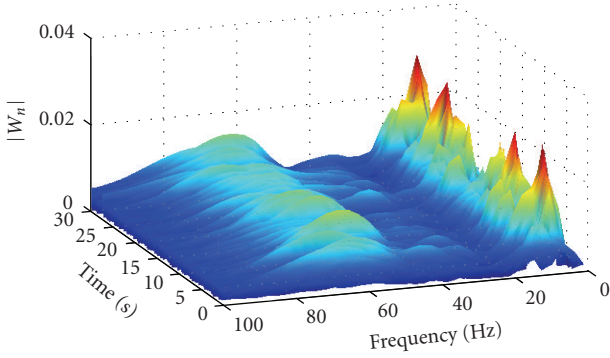
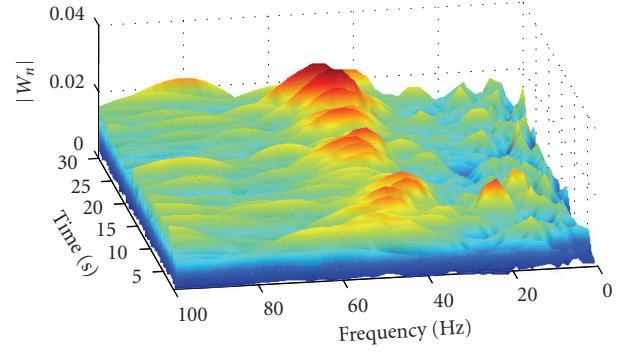
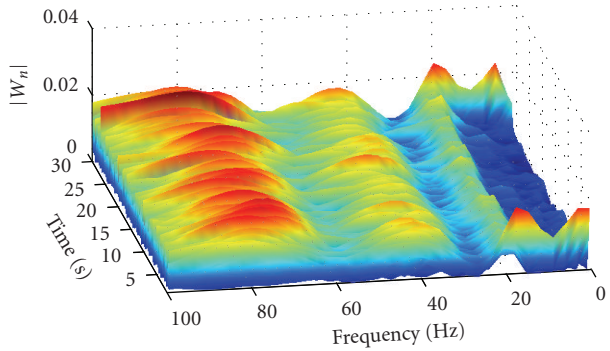
Table 2 reports some of the identified nonlinear interaction components.

The pressure pulsation at a frequency of 5 Hz was independent of the impeller velocity and it was also identified with the impeller not running (Figure 6). The intensity of the phenomenon was observed mainly in the inlet duct with a wavelet magnitude characterized by a variable value for the whole time interval. For these reasons, it appeared to be associated with system fluctuations, and in particular, with the random fluctuation of the water level in the accumulation tank of the pump.

The pressure pulsation at $St_F = 0.664$ (38.75 Hz at 500 rpm and 46.5 Hz at 600 rpm) appeared to have an internal fluid-dynamical origin, due to the absence of

TABLE 2: Some identified nonlinear interaction components.

500 rpm				600 rpm			
St	Nonlinear components	St	Nonlinear components	St	Nonlinear components	St	Nonlinear components
0.064	$St_F - 7St_S$	1.093	$St_F + 5St_S$	0.164	$St_F - 7St_S$	1.021	$St_F + 5St_S$
0.336	$St_{BPF} - St_F$	1.264	$St_F + 7St_S$	0.336	$St_{BPF} - St_F$	1.164	$St_F + 7St_S$
0.493	$St_F - 2St_S$	1.157	$2St_F - 2St_S$	0.521	$St_F - 2St_S$	1.185	$2St_F - 2St_S$
0.750	$St_F + St_S$	1.664	$St_F + St_{BPF}$	0.736	$St_F + St_S$	1.664	$St_F + St_{BPF}$
0.835	$St_F + 2St_S$	2.227	$4St_F - 5St_S$	0.807	$St_F + 2St_S$	2.300	$4St_F - 5St_S$
0.971	$2St_F - 5St_S$	2.328	$St_{BPF} + 2St_F$	0.971	$2St_F - 5St_S$	2.328	$St_{BPF} + 2St_F$
0.899	$5St_{BPF} - 6St_F$	2.664	$2St_{BPF} + St_F$	1.014	$5St_{BPF} - 6St_F$	2.664	$2St_{BPF} + St_F$

FIGURE 6: Wavelet magnitude $|Wn|$ in the inlet duct (traverse 10) with impeller no running.FIGURE 8: Wavelet magnitude $|Wn|$ in the dynamo for $Q/Q_{Des} = 100\%$ ($n = 600$ rpm).FIGURE 7: Wavelet magnitude $|Wn|$ in the dynamo for $Q/Q_{Des} = 100\%$ ($n = 500$ rpm).

these frequencies in the spectra of the not running pump (Figure 6) and in the dynamo vibrations (Figures 7 and 8).

The fluid-dynamical unsteadiness is well highlighted by the time-frequency analysis at all the flow rates. For $Q/Q_{Des} = 100\%$, the wavelet transforms were characterized by great and quite constant values for the frequency at $St_F = 0.664$ for all the transducers positioned in the diffuser blade (Figure 9). At part load, the magnitude progressively became not constant in the time domain (Figure 10). The differences of the power level were greater at low flow rates and diminished increasing the flow rate up to the design conditions.

The passage of an energy core, having a varying energy level was supposed to generate the pulsating behavior of the structure, as seen by the wavelet analysis. The energy core was associated with one of the zones of jet and wake, localized at the impeller discharge. As these zones pass over the transducers, they could be perceived as pressure fluctuations, pulsating in time and rotating around the impeller discharge.

The numerical analysis showed that at low flow rate the wake zone was characterized by sequences of vortices. The vortices, originated at about mid cord, evolved growing along the blade length up to a maximum to be reabsorbed subsequently (Figure 11). This sequence, which is comparable with a stall, generated a remarkable pressure pulsation with a period of about $3/14$ of the impeller revolution, that is, a Strouhal number equal to about 0.66.

It seemed that the modes, constituting the unsteady pattern, interfered with one another alternately in a constructive and destructive way. The resulting structure was not frozen in time, but it changed with a pulsating behavior, appearing and disappearing, depending on the interference of its modes (Figure 10).

At design flow rate, the numerical analysis did not highlight a well-defined wake zone, but the investigation of the impeller blade load showed pressure fluctuations due to both the stator rotor interaction and an independent source. In Figure 12, the pressure on the impeller blade pressure side is plotted as a function of the time and of the radius. The passage in front of the diffuser blades (DB) is marked with broken lines. The pressure evolution could be explained,

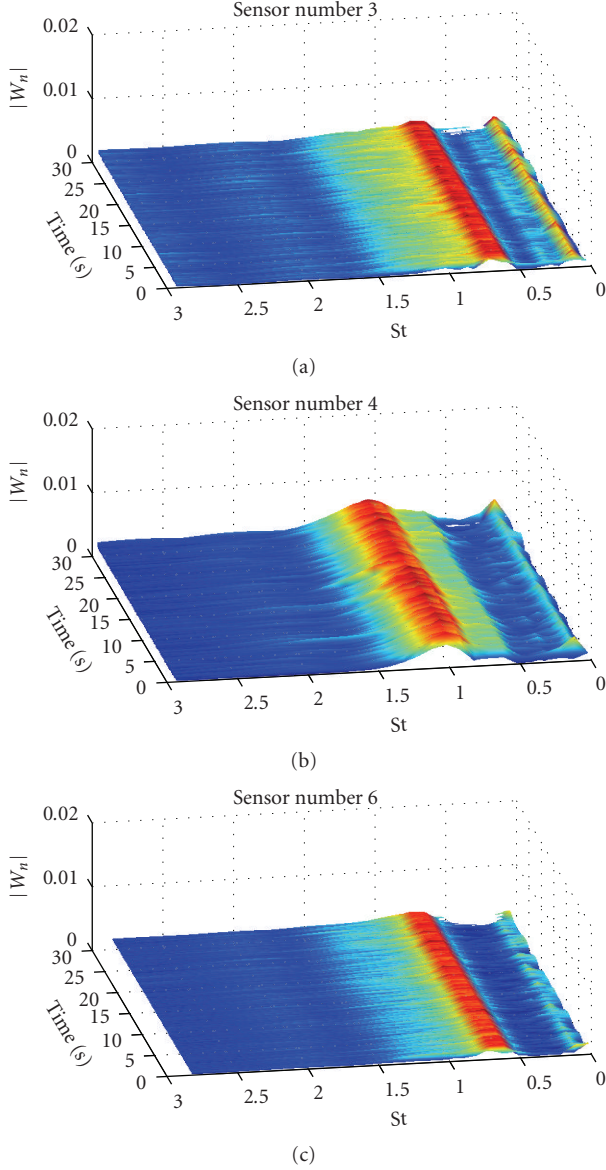


FIGURE 9: Wavelet magnitude $|Wn|$ for $Q/Q_{Des} = 100\%$ ($n = 500$ rpm).

making the hypothesis of a superimposition between the diffuser blade passage frequency (DBF = 220 Hz at 600 rpm) and a pressure pulsation with a frequency that is quite a half of the DBF.

In the relative system of reference, the Strouhal number could be expressed by

$$St_{Relative} = \frac{m}{n_b} - St_{Absolute}. \quad (10)$$

Cavazzini [24], demonstrated that the number of modes m , matching $St = 0.664$, was 15. Therefore, the relative frequency corresponding to these pulsations is 103.8 Hz at 600 rpm, that is, about 47% of the DBF. It appears to be

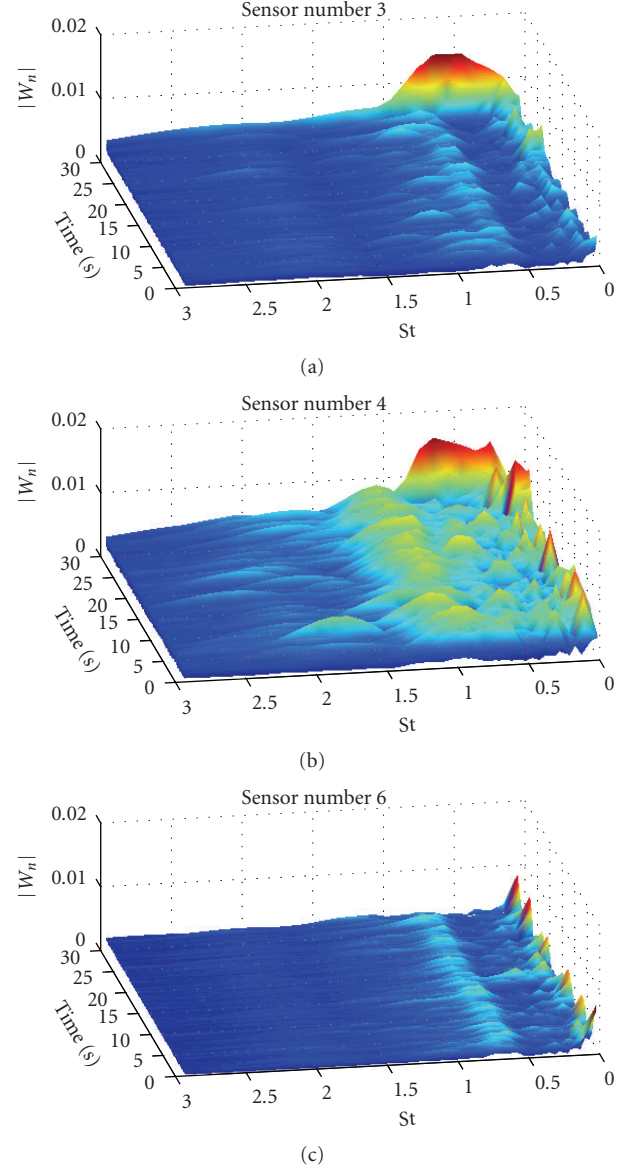


FIGURE 10: Wavelet magnitude $|Wn|$ for $Q/Q_{Des} = 48\%$ ($n = 500$ rpm).

in good accord with the identified pattern in the numerical analysis.

The mode of each blade interfered weakly with the others constituting a well-defined global pattern (Figure 9).

The frequency of the unsteady pattern ($St_F = 0.664$), as well as several of its nonlinear interaction components, had high cross-spectrum values and coherence levels greater than 0.6 for all the flow rates (Figure 13), confirming a continuous propagation of the pressure pulsations of the unsteady pattern inside the impeller.

The presence of the BPF was not always well defined, and its magnitude was often less than that of the other frequencies (Figures 4, 5, 9, and 10). A possible explanation for the low BPF amplitude could be, on one hand, the shadow effect of the diffuser blade on the transducer located

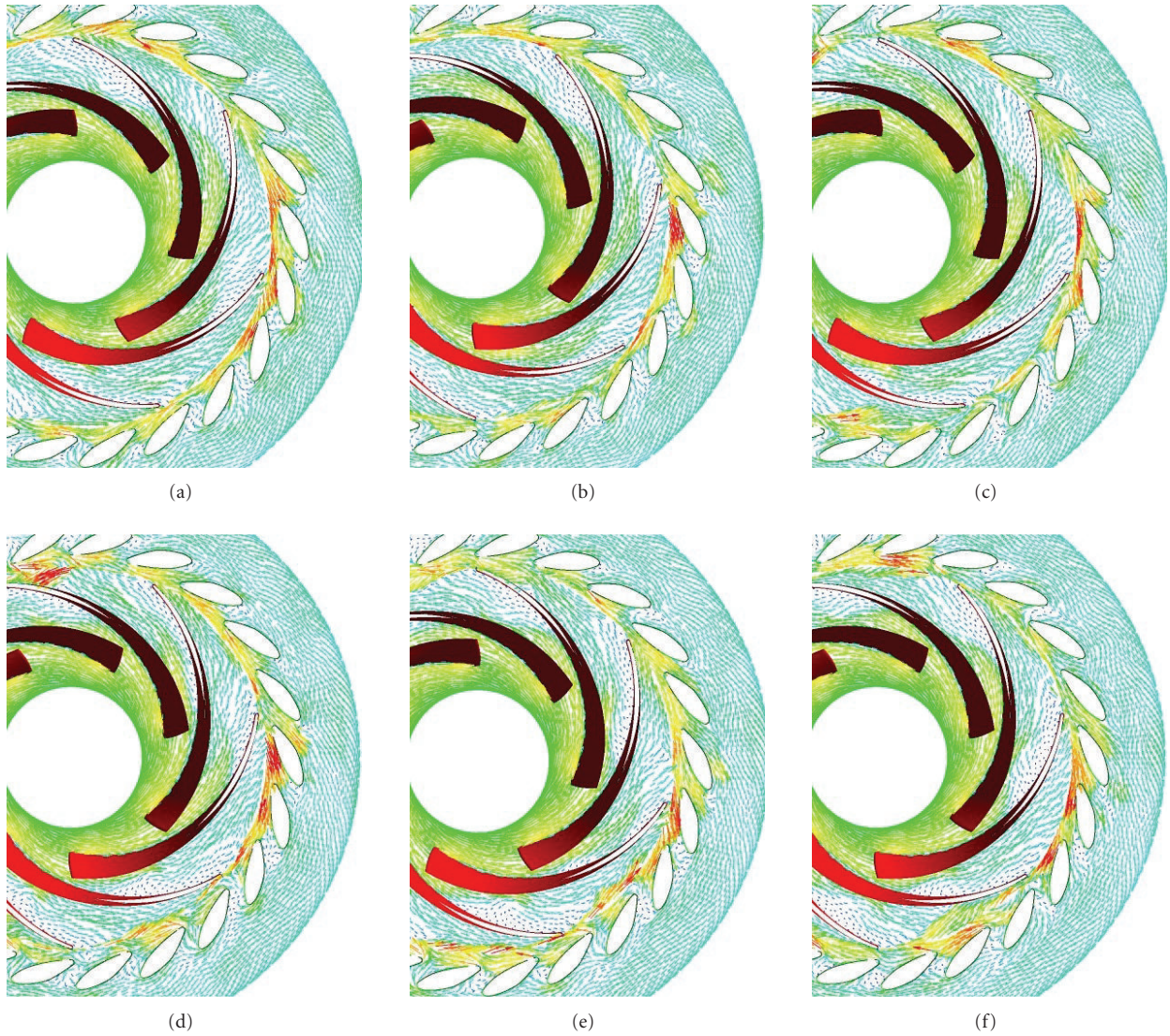


FIGURE 11: Vector plot at 10% blade height $Q/Q_{Des} = 50\%$ ($n = 600$ rpm).

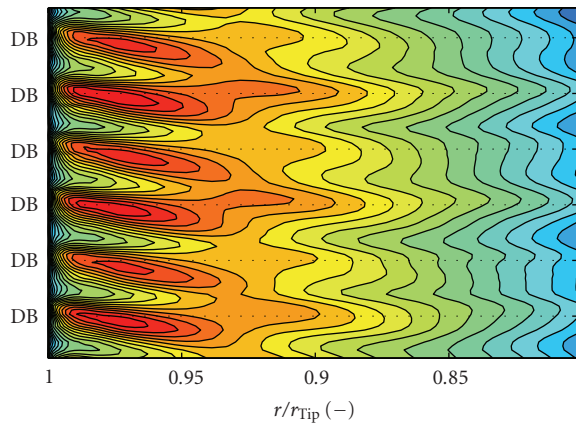


FIGURE 12: Pressure evolution in the impeller mid height for $Q/Q_{Des} = 100\%$ ($n = 600$ rpm) (DB: relative diffuser blade passage).

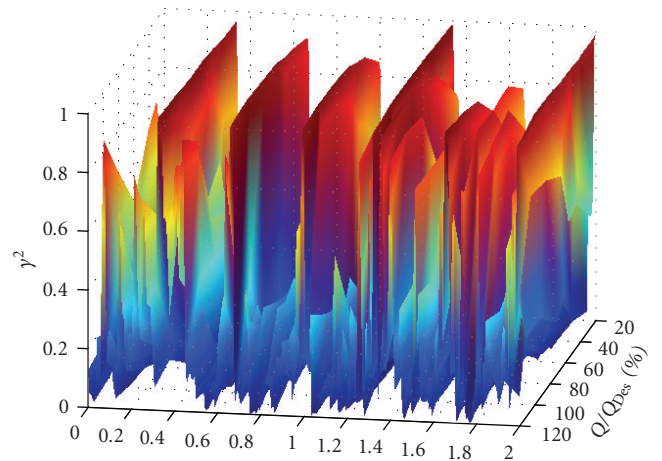


FIGURE 13: Coherence level between inlet (traverse 10) and impeller discharge (traverse 20) ($n = 600$ rpm).

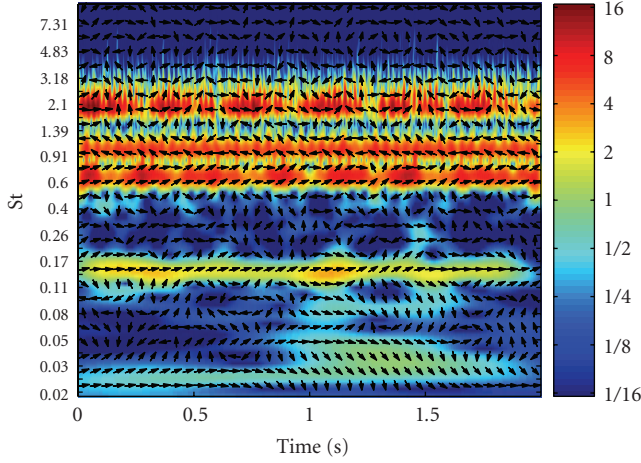


FIGURE 14: Cross-wavelet transform between the pressure transducers in traverse 20 and in position 4 for $Q/Q_{Des} = 120\%$ ($n = 600$ rpm).

on the suction side and close to the trailing edge, on the other, the existence of the unsteady pattern that determined a “natural” manipulation of the spectral content, lowering the BPF intensity [25]. Moreover, when the BPF was identifiable, it appeared to be pulsating as well as the frequencies of the unsteady pattern. This apparent pulsating behavior could be explained by the proximity of harmonics of the unsteady pattern and of a nonlinear interaction component (see Table 2) collectively with the limited resolution in the frequency domain of the wavelet transform due to the Heisenberg uncertainty.

In regards to the phase displacement, Figure 14 highlights a time-independent phase coincidence of the first harmonic of the pattern ($St = 0.664$) and an antiphase behavior in the range between $St = 0.91$ and $St = 1.13$. In this figure the arrows represent the relative phase relationship. The in-phase relation was presented as arrows pointing right, the antiphase relation as arrows pointing left, and the 90° phase displacement as arrows pointing straight on.

6. CONCLUSIONS

Experimental and numerical analyses were carried out on the flow field instability in an impeller, coupled with a vaned diffuser to study the characteristics and the development of the unsteady phenomena. Acoustic measurements were acquired by means of pressure transducers, placed in the inlet duct and at the impeller discharge, and in a diffuser vane, for two different impeller rotation velocities, in order to identify the pulsating phenomena, to define their characteristics, and to evaluate their evolution and the influence of the impeller rotation velocity on their characteristics.

The pressure signals were processed by the spectral analysis in the frequency and in the time-frequency domains to obtain information about the evolution at the time of the phenomena.

The analysis of the pressure signals highlighted the presence of a first pulsating phenomenon with a low frequency ($St = 0.071$), identified without the pump running. For these characteristics, it was associated with the system fluctuations and in particular, with the fluctuations of the water level in the accumulation tank of the pump. This hypothesis was strengthened by its greater intensity in the inlet duct.

On the other side, at the impeller discharge, a rotating structure of pressure pulsations was identified with the fundamental frequency at $St \cong 0.664$ that was not associated with the blade passage frequency (BPF). It was probably due to the pulsating wake zone at the impeller discharge resulting in a continuous propagation of the pressure pulsations of the unsteady pattern inside the impeller.

Interaction with both the blade passage frequency and with the system fluctuations generated nonlinear interaction components in the spectra, appearing and disappearing in time with regular intervals. The resulting structure was not frozen in time; it changed with a pulsating behavior, depending on the constructive or destructive interference of its constituting modes.

The numerical analyses seem to confirm the existence of this unsteady pattern and to detect the fluid-dynamical origin in the blade load as in the jet-wake instability.

NOMENCLATURE

B :	Width [m]
C_a, C_m, C_r :	Axial, meridional, and radial absolute velocity components, respectively [m/s]
D :	Diameter [m]
F :	Frequency [Hz]
G :	Gravitational constant [m/s ²]
$G_{xy}(f)$:	Elements of the cross-spectra matrices
H :	Pump head [m]
M :	Azimuthal mode number [-]
N :	Shaft speed [s ⁻¹]
N :	Number of time history segments
n_b :	Number of blades [-]
$n_s = n(Q^{0.5}/h^{0.75})$:	Specific speed [m ^{0.75} s ^{-1.5}]
P :	Pressure [Pa]
Q :	Flow rate [m ³ /s]
$St = (\pi D_2/n_b)(f/U_2)$:	Strouhal number based on the impeller tip speed [-]
U :	Peripheral velocity [m/s]
X_k :	Fourier transform data segment
y^+ :	Nondimensional variable based on the distance from the wall to the first node [-]
$W(s, n)$:	Continuous wavelet transform
W_H :	Weighting constant corresponding to the Hanning window
$W_{xy}(s, n)$:	Cross-wavelet spectrum
β :	Relative flow angle [rad]
γ :	Phase angle [°]

$\gamma^2(f)$:	Coherence function
η :	Overall efficiency [-]
$\varphi = C_{m2}/U_2$:	Flow coefficient [-]
$\phi(s, n)$:	Cross-wavelet phase difference
ω :	Angular rotation speed [s^{-1}]
ω_p :	Angular propagation speed [s^{-1}]
τ :	Time delay [s].

SUBSCRIPTS

1:	Rotor blade leading edge
2:	Rotor blade trailing edge
3:	Diffuser blade leading edge
C:	Of the blade mean line
Des:	Design
K:	Indices in equations
N:	Indication of a discrete-time signal; also specific time index of such a signal.

REFERENCES

- [1] N. Arndt, A. J. Acosta, C. E. Brennen, and T. K. Caughey, "Rotor-stator interaction in a diffuser pump," *Journal of Turbomachinery*, vol. 111, no. 3, pp. 213–221, 1989.
- [2] N. Arndt, A. J. Acosta, C. E. Brennen, and T. K. Caughey, "Experimental investigation of rotor-stator interaction in a centrifugal pump with several vaned diffusers," *Journal of Turbomachinery*, vol. 112, no. 1, pp. 98–108, 1990.
- [3] A. Furukawa, H. Takahara, T. Nakagawa, and Y. Ono, "Pressure fluctuation in a vaned diffuser downstream from a centrifugal pump impeller," *International Journal of Rotating Machinery*, vol. 9, no. 4, pp. 285–292, 2003.
- [4] S. Guo and Y. Maruta, "Experimental investigations on pressure fluctuations and vibration of the impeller in a centrifugal pump with vaned diffusers," *JSME International Journal Series B*, vol. 48, no. 1, pp. 136–143, 2005.
- [5] M. El Hajem, A. Akhras, R. Morel, and J.-Y. Champagne, "Rotor-stator interaction in a centrifugal pump equipped with a vaned diffuser," in *Proceedings of the 4th European Conference on Turbomachinery, Fluid Dynamics and Thermodynamics*, pp. 809–817, Firenze, Italy, March 2001.
- [6] A. Akhras, M. El Hajem, J.-Y. Champagne, and R. Morel, "The flow rate influence on the interaction of a radial pump impeller and the diffuser," *International Journal of Rotating Machinery*, vol. 10, no. 4, pp. 309–317, 2004.
- [7] M. Sinha, J. Katz, and C. Meneveau, "Quantitative visualization of the flow in a centrifugal pump with diffuser vanes—II: addressing passage-averaged and large-eddy simulation modeling issues in turbomachinery flows," *Journal of Fluids Engineering*, vol. 122, no. 1, pp. 108–116, 2000.
- [8] G. Wuibaut, G. Bois, P. Dupont, G. Caignaert, and M. Stanislas, "PIV measurements in the impeller and the vaneless diffuser of a radial flow pump in design and off-design operating conditions," *Journal of Fluids Engineering*, vol. 124, no. 3, pp. 791–797, 2002.
- [9] N. A. Cumpsty, "Review: a critical review of turbomachinery noise," *Journal of Fluids Engineering*, vol. 1, no. 2, pp. 278–293, 1977.
- [10] W. Neise, "Noise reduction in centrifugal fans: a literature survey," *Journal of Sound and Vibration*, vol. 45, no. 3, pp. 375–403, 1976.
- [11] L. G. Mongeau, *Experimental study of the sound generation by rotating stall in centrifugal turbomachines*, Ph.D. thesis, The Pennsylvania State University, University Park, Philadelphia, Pa, USA, May 1991.
- [12] L. Mongeau, D. E. Thompson, and D. K. McLaughlin, "Sound generation by rotating stall in centrifugal turbomachines," *Journal of Sound and Vibration*, vol. 163, no. 1, pp. 1–30, 1993.
- [13] J.-S. Choi, *Experiment on the unsteady flowfield associated with the noise generation in a centrifugal turbomachinery*, Ph.D. thesis, The Pennsylvania State University, University Park, Philadelphia, Pa, USA, December 1991.
- [14] J.-S. Choi, D. K. McLaughlin, and D. E. Thompson, "Experiments on the unsteady flow field and noise generation in a centrifugal pump impeller," *Journal of Sound and Vibration*, vol. 263, no. 3, pp. 493–514, 2003.
- [15] P. Bent, *Experiments on the aerodynamic generation of noise in centrifugal turbomachinery*, Ph.D. thesis, The Pennsylvania State University, University Park, Philadelphia, Pa, USA, May 1993.
- [16] G. Ferrara, L. Ferrari, and L. Baldassarre, "Rotating stall in centrifugal compressor vaneless diffuser: experimental analysis of geometrical parameters influence on phenomenon evolution," *International Journal of Rotating Machinery*, vol. 10, no. 6, pp. 433–442, 2004.
- [17] L. Horodko, "Identification of rotating pressure waves in a centrifugal compressor diffuser by means of the wavelet cross-correlation," *International Journal of Wavelets, Multiresolution and Information Processing*, vol. 4, no. 2, pp. 373–382, 2006.
- [18] L. Horodko, "Detection of surge precursors in a centrifugal compressor with a wavelet method," in *Proceedings of the 7th European Conference on Turbomachinery, Fluid Dynamics and Thermodynamics*, Athens, Greece, March 2007.
- [19] G. Ardizzon and G. Pavesi, "Analysis of unsteady flow in a vaned diffuser radial flow pump," in *Proceedings of the 10th International Symposium on Transport Phenomena and Dynamics of Rotating Machinery (ISROMAC '04)*, Honolulu, Hawaii, USA, March 2004, ISROMAC10-2004-084.
- [20] M. Farge, "Wavelet transforms and their applications to turbulence," *Annual Review of Fluid Mechanics*, vol. 24, no. 1, pp. 395–457, 1992.
- [21] H. Li, "Identification of coherent structure in turbulent shear flow with wavelet correlation analysis," *Journal of Fluids Engineering*, vol. 120, no. 4, pp. 778–785, 1998.
- [22] C. Torrence and G. P. Compo, "A practical guide to wavelet analysis," *Bulletin of the American Meteorological Society*, vol. 79, no. 1, pp. 61–78, 1998.
- [23] C. Torrence and P. J. Webster, "Interdecadal changes in the ENSO-monsoon system," *Journal of Climate*, vol. 12, no. 8, pp. 2679–2690, 1999.
- [24] G. Cavazzini, *Experimental and numerical investigation of the rotor-stator interaction in radial turbomachines*, Ph.D. thesis, University of Padova, Padova, Italy, 2006.
- [25] O. Akin and D. Rockwell, "Actively controlled radial flow pumping system: manipulation of spectral content of wakes and wake-blade interactions," *Journal of Fluids Engineering*, vol. 116, no. 3, pp. 528–536, 1994.



Hindawi

Submit your manuscripts at
<http://www.hindawi.com>

